Dynamics of an optically confined nanoparticle diffusing normal to a surface

Perry Schein,[1] Dakota O'Dell,[2] and David Erickson[1,*]
[1]*Sibley School of Mechanical and Aerospace Engineering, Cornell University, Ithaca, New York 14853, USA*
[2]*School of Applied and Engineering Physics, Cornell University, Ithaca, New York 14853, USA*
(Received 10 May 2016; published 27 June 2016)

Here we measure the hindered diffusion of an optically confined nanoparticle in the direction normal to a surface, and we use this to determine the particle-surface interaction profile in terms of the absolute height. These studies are performed using the evanescent field of an optically excited single-mode silicon nitride waveguide, where the particle is confined in a height-dependent potential energy well generated from the balance of optical gradient and surface forces. Using a high-speed CMOS camera, we demonstrate the ability to capture the short time-scale diffusion dominated motion for 800-nm-diam polystyrene particles, with measurement times of only a few seconds per particle. Using established theory, we show how this information can be used to estimate the equilibrium separation of the particle from the surface. As this measurement can be made simultaneously with equilibrium statistical mechanical measurements of the particle-surface interaction energy landscape, we demonstrate the ability to determine these in terms of the absolute rather than relative separation height. This enables the comparison of potential energy landscapes of particle-surface interactions measured under different experimental conditions, enhancing the utility of this technique.

DOI: 10.1103/PhysRevE.93.062139

I. INTRODUCTION

Nanoparticles with diameters smaller than 1 μm are being increasingly used for numerous commercial and industrial applications, including drug delivery [1], enhanced oil and gas recovery [2], and cosmetics [3]. Many of these applications require nanoparticles to operate in environments where they are tightly confined in regions with characteristic particle-wall separation distances on the scale of the particle diameter, such as geological pores and *in vivo* capillaries. In these regions, the hydrodynamic effects of the wall play an important role in dictating the transport properties of the nanoparticles.

Theoretical studies of the motion of small particles near fluid-solid interfaces were carried out in the 1960s by Brenner and co-workers [4–7], who derived an exact expression for the dependence of the diffusion coefficient in the direction perpendicular to the surface as a function of particle size and separation distance. For regions near the interface (small h/R), Brenner's exact solution can be approximated [7,8] and the scaling factor is given as

$$\frac{D_\perp}{D_{\text{bulk}}} = f_\perp^{-1},$$
$$f_\perp \approx \frac{R}{h} + 0.2\ln\left(\frac{R}{h}\right) + 0.9712, \tag{1}$$

where $D_\perp$ is the local diffusion coefficient in the perpendicular direction, D_{bulk} is the bulk diffusion coefficient far from the wall, $f_\perp$ is the scaling factor, R is the particle radius, and h is the distance from the bottom of the particle to the interface. The full solution, along with this approximation, are plotted in Fig. 1(a).

Over the decades since Brenner's theory was published, there have been numerous experimental studies of the motion of particles near a wall providing evidence in support of the theory, initially on millimeter [9] scale particles before moving to the micrometer scale [10–12]. Many of these studies have used total internal reflection microscopy (TIRM) to measure the hydrodynamically hindered particle motion under various conditions [13–16]. A noteworthy example of this is the study performed by Oetama and Walz [17], who directly measured the motion of 15-μm-diam particles about 50–100 nm from a surface. This was achieved by looking at many trajectories of a single particle from each height and computing the variance in particle displacement following short time lags, and relating this to the local diffusion coefficient. Once this was done for several particle heights, the $D_\perp$ curve was fit to a linear approximation of Brenner's series [see the black curve in Fig. 1(a)] allowing the absolute particle separation distance to be determined.

However, there are challenges involved in scaling this method to the nanoparticle regime. This is illustrated in Fig. 1(b). For 15-μm-diam particles, the linear approximation is reasonable. However, for nanoparticles at similar separation heights, this approximation breaks down and more accurate approximations are needed, as illustrated by the divergence of the black curve from the red and blue curves for the $R = 400$ nm case in Fig. 1(b). Indeed, most of the experimental studies on hindered diffusion are performed for very small h/R ratios. Another challenge in directly measuring the diffusive motion of smaller particles is that the bulk diffusion coefficient is inversely proportional to particle size. As a result, most of the previous work in this field has been limited to micrometer scale particles. A recent study by Liu *et al.* [18] looked at the diffusion of 3-μm-diam particles near an evanescently illuminated surface by holding them in place vertically using optical tweezers combined with a TIRM setup. Their experimentally measured diffusion coefficients match the predictions of Brenner's theory over a wide separation range from contact with the surface to about $h/R = 1$. While this measurement is useful as a system calibration allowing for the calculation of absolute separation distances without knowledge of system

*de54@cornell.edu

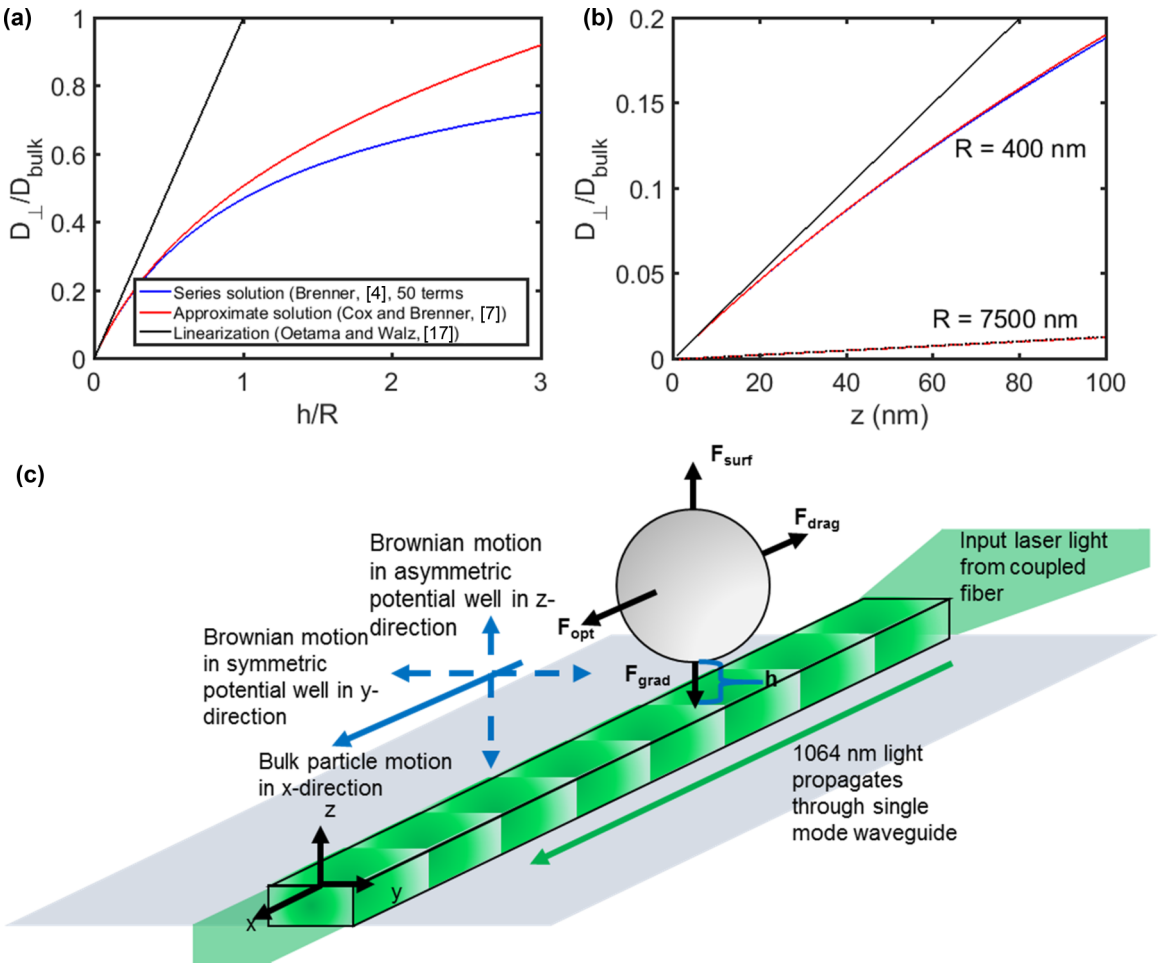

FIG. 1. (a) Nondimensionalized plot illustrating Brenner's series solution (blue line, see also [4]) as well as some simplified approximations (red [7] and black lines [17]) for the fraction of bulk diffusion coefficient in the direction normal to a surface as a function of separation height (normalized by particle radius). (b) Fraction of bulk diffusion coefficient plotted as a function of height for separation distances within 100 nm of a wall. Colors same as in the legend; solid lines correspond to a particle with $R = 400$ nm studied here, while dashed lines correspond to a particle with $R = 7500$ nm. (c) Schematic of the experimental force picture and resulting three-dimensional motion.

parameters such as the evanescent penetration depth, the total measurement time needed to generate the $D_\perp$ curve for one particle was 20 min, making this technique poorly suited for high-throughput particle characterization.

Here we study the motion of submicrometer diameter particles as they undergo hindered diffusion near a liquid-solid interface. We demonstrate the capability of measuring the diffusion coefficient normal to the surface and determining the absolute particle-surface separation heights. This allows for population level particle-surface interaction measurements from a single-particle basis, enabling the identification of subpopulations in a heterogeneous suspension and the direct comparison of nanophotonic force microscopy (NFM) [19] measurements under different experimental conditions with different equilibrium positions. Using a waveguide architecture, we measure particles sequentially with high-throughput with measurement times as short as 5 s per particle. The optical gradient force generated by the waveguide pulls the nanoparticles close enough to the surface to measure, while the high-speed CMOS camera enables measurement of the local diffusion coefficient at short enough time scales to neglect the drift effects.

II. ANALYSIS PROCEDURE

The experimental system used in this study consists of a single-mode silicon nitride rectangular waveguide. Suspensions containing nanoparticles flow over this waveguide in a microfluidic channel. For details of the experimental apparatus, please see Sec. V. As particles in the suspension interact with the waveguide, they experience forces and resulting drift motion in three dimensions, in addition to Brownian motion, as illustrated schematically in Fig. 1(c). In the x direction, along the optical axis of the waveguide, the particle experiences a propulsion force given by the sum of optical absorption and scattering balanced by the hydrodynamic drag force [20]. In the y direction, the particle experiences a symmetric potential that can be modeled as harmonic due to the restoring force provided by the optical gradient along the cross-sectional mode profile. In the z direction, normal to the surface, the particle experiences an optical gradient force in the direction toward the waveguide due to the exponential gradient in the evanescent field. This is balanced by the net particle-surface interaction forces (e.g., electrostatic repulsion in a screened electrical double layer). The optical gradient force, F_{grad}, is

computed as [21]

$$F_{\text{grad}} = \frac{2\pi\alpha_p}{c}\nabla I, \tag{2}$$

where α_p is the polarizability of the particle, c is the speed of light, and ∇I is the intensity gradient. Unlike the TIRM scenario described previously, the fiber-coupling scheme provides a fixed angle of incidence, and the evanescent penetration depth is a known system parameter. As the particle moves along the waveguide and interacts with the evanescent field, it scatters light. The amount of light scattered depends exponentially on its height:

$$I_{\text{scat}} = I_o \exp(-z/d_p), \tag{3}$$

where I_{scat} is the light scattered by the particle measured by the camera, I_o is the light that a particle at $z = 0$ would scatter, and d_p is the evanescent penetration depth. In practice I_o is not known, and it will be different for every particle in a polydisperse sample, as it is a strong function of particle size. This is especially true for particles in the Mie regime, where the particle size is comparable to or larger than the optical wavelength, and morphology-dependent resonances can occur [22]. However, without knowing I_o, the change in height of a single particle between two different observations can be determined by taking the ratio of I_{scat}. When many observations of a particle are taken, as in our experiments, it becomes convenient to compute the position of the particle in each frame relative to some reference height. In our previous work, we used the equilibrium position as this reference [19]. Here, with the eventual goal of determining these separation heights absolutely, we take a different approach, based on one developed previously in the literature [17]. Briefly, we select an arbitrary value of $I_o, I_{o,\text{guess}}$, define the particle position in all frames based on this guess, and compute the trajectory $z(t)$. It follows from Eq. (3) that

$$\begin{aligned} I_{\text{scat}}(t) &= I_{o,\text{guess}} \exp[-z_{\text{relative}}(t)/d_p], \\ z_{\text{absolute}}(t) &= z_{\text{relative}}(t) + z_{\text{offset}}, \end{aligned} \tag{4}$$

where z_{absolute} is the actual distance from the bottom of the particle to the waveguide, z_{relative} is the height relative to where $I_{\text{scat}} = I_{o,\text{guess}}$, and z_{offset} is an unknown constant for each particle that will be determined through fitting the experimental data to hydrodynamic models.

To analyze the dynamics of our system, we begin by writing the stochastic equation of motion for a particle moving near the waveguide. While the particle motion along the waveguide is a three-dimensional process [see Fig. 1(c)], here we will decouple the motion in the z direction. Unlike previous works, the particles that we are studying are subjected to drift due to near-field optical gradient forces in the evanescent fields; at short time scales these become unimportant, and an approach resembling that developed in the prior literature can be used [17]. Using this Langevin-equation [8] approach, the one-dimensional equation of motion in the z direction for our system can be written as

$$\begin{aligned} \Delta z = {} & \frac{D_\perp(z)}{k_B T}(F_{\text{grad}} + F_{\text{surf}})\Delta t \\ & + \frac{dD_\perp(z)}{dz}\Delta t + W(t)\sqrt{2D_\perp(z)\Delta t}, \end{aligned} \tag{5}$$

where Δz is the vertical displacement, F_{surf} is the net particle-surface interaction force, and $W(t)$ is a random variable chosen from the normal distribution with a mean of zero and a variance of 1. If the displacement is small, we can simplify this expression by taking $D_\perp(z) = D_{\text{app}}$, the apparent diffusion coefficient observed for motion near position z, which is valid if the particle moves a small enough distance that the change in the diffusion coefficient is negligible. This can be ensured by taking a small enough Δt that the particle does not have time to displace very far. In the limit of small Δt, further simplifications can also be made because the drift term due to external forces and the diffusivity gradient term both scale with Δt while the fluctuation term scales with $\sqrt{\Delta t}$ and thus it decays less rapidly as the lag time is decreased. In this diffusion-dominated regime, the displacement depends only on the fluctuation term:

$$\Delta z \approx W(t)\sqrt{2D_{\text{app}}\Delta t}. \tag{6}$$

By the definition of $W(t)$, the variance of the distribution of observed Δz is

$$\sigma_z^2 = 2D_{\text{app}}\Delta t \tag{7}$$

so D_{app} at a given height can be determined by plotting the variance in the displacement over many vertical displacement "jumps" from that height as a function of the jump time lag, Δt, and taking the slope.

To estimate z_{offset} and therefore calculate z_{absolute}, we seek to determine the apparent diffusion coefficient at several heights and fit it to the approximation of Brenner's series. Since the diffusion coefficient is spatially dependent and will change over the course of each particle's trajectory, and this process is influenced over long times by drift forces that are spatially dependent as well, we look at what happens over short vertical jumps from when a given height is sampled. Due to the stochastic nature of the process, we need to make a statistical measurement incorporating many jump trials from an initial height. To increase the number of jumps used in the statistics, we incorporate an approach that trades off some of the position resolution in order to obtain large statistical sampling while maintaining throughput. This is accomplished by discretizing the data to reduce the number of initial heights used and increase the number of trajectories from each height (see Sec. V for details).

III. RESULTS

A. Variance in separation height

Figure 2 shows the results of a typical experiment. In Fig. 2(a), for trajectories from one height that the system stochastically samples, we compute the variance in the displacement after a given lag time. The lag times used are integer multiples of the period between camera acquisitions, in this case (1/3000) s. The black curve and symbols represent the experimental data, while the red dashed line is a linear fit of the first three data points. The slope of this red line corresponds to the apparent diffusion coefficient, as shown in Eq. (7). The short time scale motion is highlighted in the inset. The linear increase is indicative of a regime in which the particle drift is negligible and diffusion dominates. The first three points are used in the fitting because this is the regime

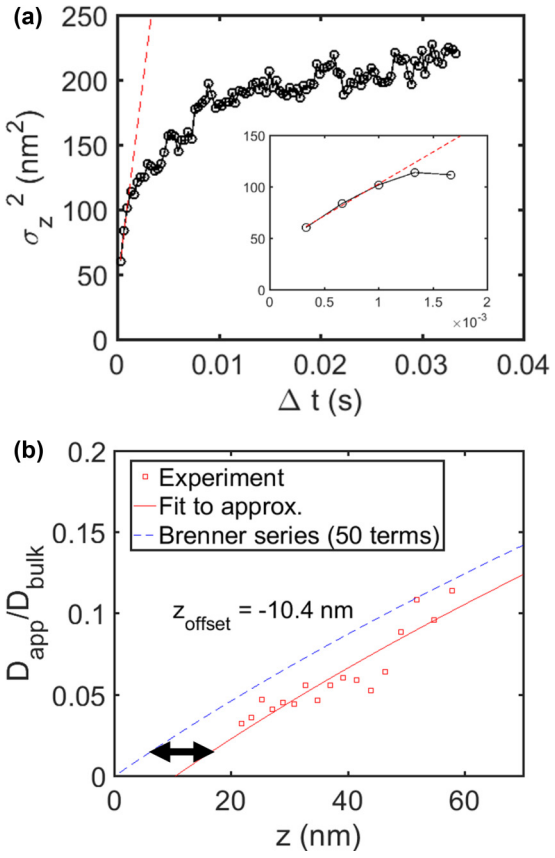

FIG. 2. (a) Variance in vertical displacement vs lag time, computed for at least 500 trajectories from a single initial condition. At short time scales, drift is negligible and the particle undergoes normal diffusion. The diffusion coefficient is computed by taking the slope of the linear fit to the first three data points (red curve). Inset: closeup of the first five data points illustrating linear fitting in the diffusion-dominated regime. (b) After effective diffusion coefficients are determined for all initial conditions with sufficient trajectories, the data are fit, and the vertical offset is computed. The red squares are the experimental data. The red curve is the fit to the data using Eq. (8). For reference, the bulk diffusion coefficient for this particle is $D_{bulk} = 6.14\times10^{-13}$ m^2/s.

where drift due to the force field is smallest and diffusive motion dominates, leading to the most accurate prediction possible with this sampling rate. As the inset shows, for short time lags the particle is in the diffusive regime and the variance in the displacement is linear, as indicated by Eq. (7). The slope decreases as drift becomes more significant. At long time scales, the particle experiences the whole potential energy well and the variance no longer changes monotonically with increasing lag time. When this procedure is repeated for different initial conditions that the particle stochastically samples, different values of D_{app} are computed, as expected from Eq. (1). These are plotted as the red open squares in Fig. 2(b). Of course, our values for the initial conditions are calculated based on an arbitrary selection of $I_{o,guess}$. To find the actual height of the particle, the experimental data are fit to a curve based on the approximation in Eq. (1), as shown in the red line in Fig. 2(b). To simplify computation, this is done using the nondimensional form of the equation, modified from Eq. (1) to include a fitting parameter for the spatial offset:

$$\frac{D_\perp}{D_{bulk}} = \left[\frac{R}{h+z_{offset}} + 0.2\ln\left(\frac{R}{h+z_{offset}}\right) + 0.9712\right]^{-1}. \quad (8)$$

The result is a shifting of the $D(z)$ curve, as shown in Fig. 2(b), annotated by the double arrow.

B. Population level energy landscape mapping

A major advantage of the waveguide architecture is the ability to interrogate particles in rapid succession to achieve high throughput. This can be observed in the supplemental movie (see the supplemental material and the Appendix for a detailed description), which depicts a single data acquisition. While not all of these particles can be tracked for long enough to get sufficient statistical data, the throughput is sufficient to obtain population level data over the course of a single experimental session (4–6 h, including setup time). The value of z_{offset} obtained from the fits to the $D(z)$ curve specify the absolute separation height between the bottom of the particle and the surface in each time step. This is useful, since the same data used in these experiments can also be used to map the potential energy landscape incorporating the interactions between the particle and the surface as well as between the particle and the evanescent field. From the distribution in intensity as the particle translates along the waveguide, the relative potential energy can be computed from the Boltzmann statistics (for details, see [23]):

$$\frac{U(z_{rel}) - U(z_{eq})}{k_B T} = \ln\left[\frac{P[I_{scat}(z_{eq})]I_{scat}(z_{eq})}{P[I_{scat}(z_{rel})]I_{scat}(z_{rel})}\right], \quad (9)$$

where $U(z)$ is the potential energy at position z, $I_{scat}(z)$ is the measured scattered light intensity, and $P[I(z)]$ is the probability of scattering at a given intensity determined from the measured distribution. However, since z_{offset} is determined from the fit, an absolute height can now be associated with each state. This facilitates the comparison of energy landscapes measured under different experimental conditions with different equilibrium heights. This is shown in Fig. 3, where we show corrected equilibrium positions under different experimental salt concentrations, in dilute KCl and phosphate buffered saline (PBS) solutions, as characterized by the Debye screening lengths (λ_D). Each plot shows all particles successfully tracked in the given experimental condition with data meeting the criteria previously discussed, particularly at least 15 000 frames of tracked data at 3000 frames per second for each particle. The particles used in all cases were NIST-traceable size standard polystyrene spheres (see details in Sec. V).

C. Direct comparisons of nanoparticle-surface interactions under different conditions

To illustrate the utility of this advance, in Fig. 4 the potential energy wells for two particles measured in different salt concentrations are shown, in 0.01× PBS ($\lambda_D = 7.6$ nm, blue squares) and in 0.001× PBS ($\lambda_D = 24$ nm, black circles). The experiments were performed on the same waveguide at approximately the same coupled optical power. The measured equilibrium is closer to the surface for the high salt case,

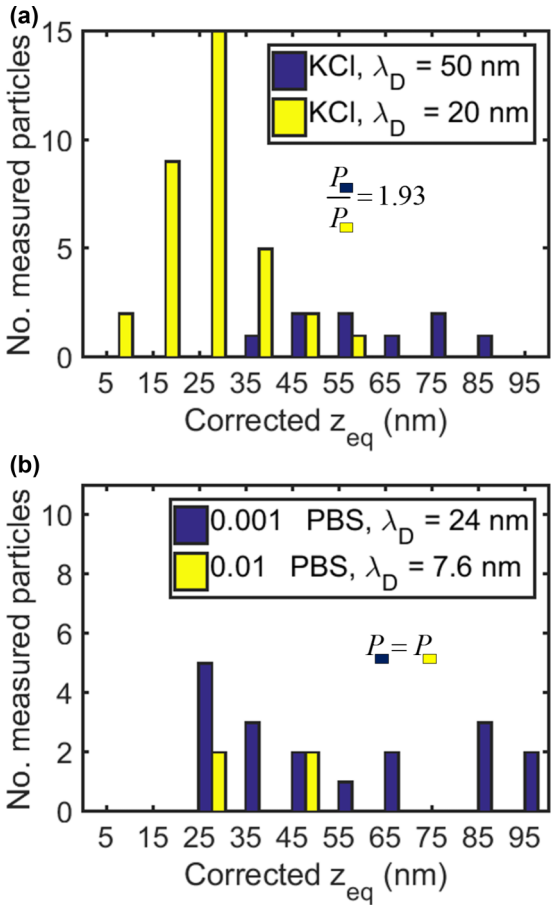

FIG. 3. Histograms illustrating the number of experimentally measured particles at each calculated corrected equilibrium height, z_{eq}, under various experimental conditions. (a) 0.076 mM KCl in deionized water, $\lambda_D = 50$ nm (blue bars), and 0.237 mM KCl in deionized water, $\lambda_D = 20$ nm (yellow bars). Note that these experiments were performed at different optical powers, P, to ensure sufficient trapping, which also influences z_{eq}. (b) PBS diluted to 0.001× in deionized water, $\lambda_D = 24$ nm (blue bars), and PBS diluted to 0.01× in deionized water, $\lambda_D = 7.6$ nm (yellow bars). These experiments were performed on the same waveguide with the same optical power.

consistent with the expectation of increased screening of the electrostatic repulsive forces due to the thinner electrical double layer. Looking at the left side of the curves, the repulsive energy barrier for reaching $z_{absolute}$ is much higher for the lower salt case, stabilizing the suspension. At higher salt concentrations, there is enhanced screening of the electrostatic repulsion, and therefore the energy barrier to coming into contact with the surface is lower. Comparing the right-hand side of both curves, the similar magnitude and shape of the curve in the optical gradient dominated regime is consistent with the similar polarizability of both particles and the same optical power being applied in both cases.

IV. DISCUSSION

Significantly, Fig. 2 indicates that with a reasonably fast camera, we are able to obtain data in the diffusive regime where

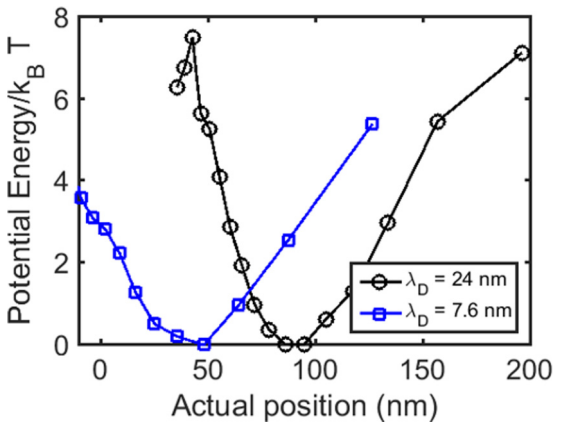

FIG. 4. Potential energy wells calculated using the Boltzmann inversion for example particles in two different salt concentrations (0.001× PBS, $\lambda_D = 24$ nm, black curve and 0.01× PBS, $\lambda_D = 7.6$ nm, blue curve). The heights (horizontal axis) are absolute distances between the particle bottom and the waveguide. The potential energy, plotted as the energy difference relative to the equilibrium position for each particle, is given in units of k_BT and includes contributions from the optical gradient and the particle-surface interaction.

the variance in the vertical displacement is proportional to the lag time of the measurement, with the slope corresponding to the effective diffusivity of the particle. In this regime, the particle has not yet had time to respond to the external forcing of the optical and electrostatic fields, and instead its motion is determined purely by hydrodynamic effects. The use of a camera capturing the scattered light is important because we are able to record both the intensity and position of the scattered light pattern as the particle is propelled along the waveguide by the optical scattering force. The optical confinement provided by the waveguide in two dimensions allows us to probe particles with diameters smaller by a factor of 20 compared to similar analytical methods used without this confinement in the past [17], while relaxing the confinement in the x direction allows for estimates of the absolute separation height with measurement times of about 5 s per particle as opposed to 20 min [18] or longer [24] with current state-of-the-art methods. The use of scattered light allows for shorter integration times, leading to measurements in the regime unbiased by drift effects, in contrast to recent studies with fluorescence techniques [25]. This is especially important when considering previous studies using near-field fluorescence techniques that report underestimating the z direction hindered diffusion of nanoparticles due to their inability to differentiate hydrodynamic effects from the electrostatic repulsion between the particle and the surface [26,27]. In our experiments, Δt is sufficiently short [see Eq. (7)] that we are able to measure the hydrodynamics of $R = 400$ nm particles, obtaining results consistent with the Brenner theory for normal diffusion in this regime.

As Fig. 2(b) shows, the estimate of z_{offset} depends primarily on the accuracy of the fit curve to the measured local diffusion coefficients. As a result, the accuracy of this value depends on how accurately the slope of the variance in vertical position represents the diffusion coefficient in the diffusion-dominated regime. This becomes more precise if more points are used in

computing the variance and more accurate when the sampling rate is fast relative to the rate of diffusion. As D is smallest closest to the interface, for larger separations this becomes less accurate because the time scale of diffusion is faster relative to the camera sampling rate. It is worth noting that as shown in Eq. (1), the diffusion coefficient is a function of both height and particle size. Therefore, in principle it is possible to obtain an estimate of particle size as well as absolute height by using two free parameters in the fitting in Eq. (8). However, the accuracy of this remains poor with the present experiments. A route forward for future investigations may be to use the absolute height estimate obtained here in conjunction with a method based on the in-plane diffusion parallel to the surface, as we did in our previous work to obtain relative changes in particle size [28].

Since the primary limit to the sampling frequency available using CMOS cameras is the data transfer rate, we predict that improved technologies (for example, the emerging USB 3.1 Generation 2 data transfer standard [29]) will enable higher frame rates, enabling measurements on smaller particles in the coming years. In addition, some progress has been made recently in extracting relevant physical parameters using data collected in the regime where both drift and diffusion effects are significant [24,30]. Accounting for drift effects will allow sampling rates that are slower relative to the diffusion time scales to still yield useful information.

Figure 3 displays histograms of the corrected equilibrium positions measured for populations of particles. This is accomplished in both 1:1 electrolyte [Fig. 3(a)] and diluted buffered solutions [Fig. 3(b)]. The data are consistent with physical expectations, as in the higher salt concentration experiments more particles have equilibrium positions closer to the surface, as expected from the increased screening of the electrostatic forces characterized by the shorter Debye length (λ_D). As the figure shows, there is some variation in the equilibrium positions measured within each experimental condition. This is likely due to the fact that this position depends on the balance of optical gradient and surface force effects, and the optical gradient force depends on the polarizability of the particle, which is a function of particle radius to the third power, which explains these variations even with such nominally monodisperse samples. However, as shown most clearly with the blue bars on the right side of Fig. 3(b), a small number of particles behave much differently than the rest of the population. This illustrates how this technique can be used for the identification of impurities or other subpopulations in a heterogeneous suspension environment.

Unlike ensemble-averaged measurement techniques such as dynamic light scattering, the presence of these different particles does not bias the results of the measurement on the primary constituents, as the individual data for each particle are measured independently. The estimation of absolute height requires no assumption about population monodispersity and is performed individually for each particle. This is accomplished without damage to or fouling of the waveguide or changing the experimental parameters, in contrast to the methods used in conventional TIRM experiments [31]. As the supplemental movie shows (see the supplemental material and the Appendix for a detailed description), the waveguide architecture allows for the interrogation of multiple particles in rapid succession. While not all particles can be tracked for long enough to acquire a sufficiently large statistical sample to perform the diffusion analysis procedure described here, the throughput is still sufficient to perform population level measurements. Each salt concentration in each panel of Fig. 3 was obtained in a single experimental session.

In conclusion, we have demonstrated direct measurement of the diffusive motion of sub-micrometer-scale spheres hindered hydrodynamically by the presence of a wall. This can be performed simultaneously with interaction force or potential energy measurements, and it provides an additional piece of information by defining an absolute separation height that is consistent with physical expectations. This is accomplished individually for each particle, making no assumptions regarding sample heterogeneity. The nondestructive nature of the absolute height estimate combined with the sequential measurements enabled by the waveguide optical scattering force and camera-based particle tracking make this technique well-suited for high-throughput population-level measurements. This can potentially be combined with other diffusion-based measurements to eventually measure the size of individual nanoparticles simultaneous to the measurements of interaction energy and absolute height.

V. METHODS

A. Experimental setup and materials

Experiments were performed using the NanoTweezer system and integrated waveguide and microchannel chips (Optofluidics Inc., Philadelphia). Light from the system's 1064 nm diode laser was coupled into silicon nitride waveguides on-chip through optical fibers. The relative position of the fibers and the chip was adjusted to maximize measured output power. Typically, 10–25% of the input power was measured at the output photodiode. Input powers between 100 and 210 mW were used to maximize trapping without sticking beads to the waveguides, depending on the salt concentration, with higher input powers used for lower salt concentrations to compensate for the reduction in screening of the electrostatic repulsive forces. The NanoTweezer pump was turned off during these experiments to reduce mechanical vibrations. Particles were injected into the inlet tubing directly using a syringe. No bulk fluid flow was imposed on the system during data acquisition. For these experiments, NIST traceable polystyrene spheres were used (Thermo Scientific, 3800-005). These particles were certified with a measured diameter of 799 ± 9 nm diameter as measured by transmission electron microscopy (TEM). Experiments were performed in several aqueous suspensions. In all cases, the beads were diluted to 0.0015% solid fraction. Experiments were performed in either KCl (Mallinckrodt Chemical, 6858-04) or Phosphate Buffered Saline (Sigma, P5493) diluted in filtered, deionized water at the concentrations stated previously.

B. Imaging, data acquisition, and processing

Images of the scattered light were recorded using a CMOS Camera (Basler, AC2000-165umNIR). The optical axis of the waveguide was aligned with the horizontal axis of the camera for maximum acquisition speed. Images were acquired over

a region of interest spanning 16 pixels in the y direction by 780 pixels in the x direction [along the waveguide; see the coordinate system in Fig. 1(c)]. Acquisition was performed over a USB 3.0 connection with a dedicated card (StarTech, PEXUSB3S25). This allowed for acquisition rates of 3000 frames per second for 8-bit monochromatic images. To minimize motion blur, an exposure time of 24 μs was used, the shortest exposure possible with this camera. Gain levels were set to maximize the intensity signal without saturation, which was typically achieved at around 12 dB, roughly half the maximum possible with this camera, though this parameter varied under different experimental conditions to ensure the use of as much of the pixel range as possible with no saturation. 80 000 frames were acquired in each acquisition set (26.67 s per set). Between data sets there were typical delays of $\backsim$3–5 min during image writing from the memory buffer to a solid-state hard drive. Typically, one to five particles were observed during each acquisition. Particle trajectories were tracked from the raw images using the MOSAIC plugin [32,33] for ImageJ. To account for artifacts in the tracking and imaging and to ensure a large statistical sample of data, only particle trajectories where the particle moved at least five pixels (corresponding to 1.375 μm) and containing at least 15 000 frames were used in the analysis. Using the centroid position from the track, the total intensity was integrated from a 12×12 pixel box around this position in each frame using MATLAB.

As the videos obtained have a pixel depth of 8 bits, and the integration is performed over a 12×12 pixel box, there are 36 864 possible values of scattered light intensity and therefore height that can be measured in each frame. This means that using the raw intensity data, each height is sampled very few times in a typical particle trace of 15 000–30 000 frames. To get around this, each measured intensity value is divided by 100, rounded to the nearest integer, and multiplied by 100, reducing the number of possible height "bins." This can be thought of as a discretization of the data. Then, the dynamic analysis is performed for each height that is sampled 500 or more times, ensuring a reliable estimate of the variance in displacement.

C. Correction for the lateral and longitudinal intensity variations

As the waveguide intensity profile is not completely uniform, in addition to the exponential changes in the scattered light intensity due to motion in the z direction, a small portion of the intensity change will be due to the particle motion in the y direction. This is not a significant correction for small particles whose radius is much smaller than that of the waveguide and in scenarios where the confinement is tighter, as in our previous work [19], but for the loosely confined 400-nm-radius particles studied in this work, this could account for a substantial portion of the intensity change. To correct for this to a first approximation, we have developed an approach based on subtracting the underlying mode profile from the lateral distribution of the intensity. This approach works as follows. The intensity data are plotted as a function of the y position, as shown in Fig. 5(a). As the figure shows, for positions near the center of the waveguide there is little correlation between the observed intensity and the lateral position in the region where the mode profile is relatively

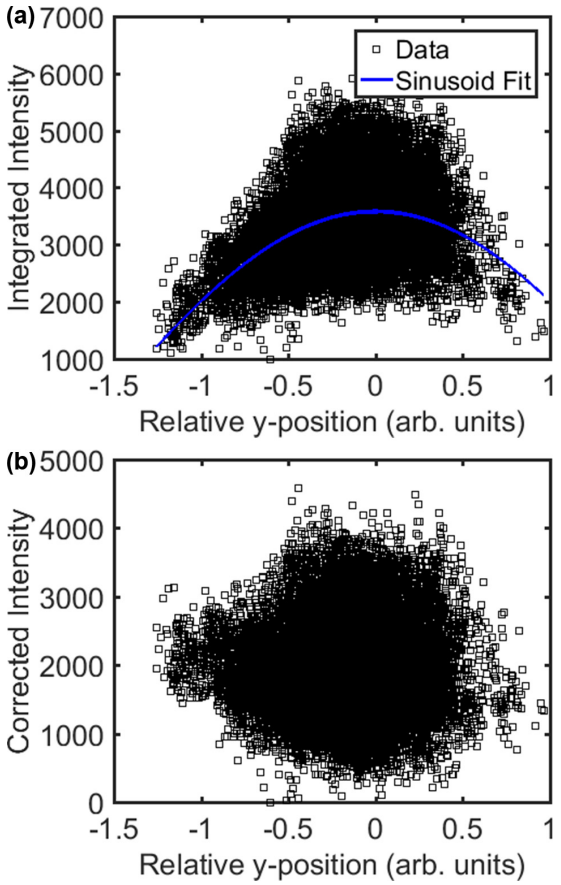

FIG. 5. Mode profile intensity correction. (a) Raw intensity data as a function of horizontal position in pixels. The blue curve is a sinusoidal fit to the data. (b) Corrected intensity following subtraction of the sinusoid and renormalization. For reference, the total range of motion of this particle in the y direction is 0.61 μm.

flat. Toward the edges, there is a stronger y dependence, and the overall range of intensities sampled is lower because there is less light available for scattering in this region. To a first approximation, the mode profile can be modeled as a sinusoid. Fitting a sinusoid to the data as in the blue curve in Fig. 5(a), note that the correlation is weak because the intensity depends much more strongly on the z position than on the y position. When this fitted curve is subtracted from the data, the result is an intensity distribution that is uncorrelated from the y position, as in Fig. 5(b). This is the data used for further analysis.

In principle, variations in the evanescent field intensity along the direction of propagation [x direction in Fig. 1(c)] can also play a role in these measurements. However, for the single-mode silicon nitride structures used here, the material scattering and absorption losses in the experimental window are quite small ($<$0.1% [34]) and the field can be considered uniform in this direction. While the presence of waveguide defects or stuck particles may locally cause the evanescent field to be nonuniform in the x direction, in practice these regions are excluded from the analysis as the tracking algorithm loses the particle as it interacts with these defects. With the waveguides used here, no significant defects with detectable scattering were observed prior to the start of experiments.

Particle sticking occurred very infrequently with the relatively low powers and moderate salt concentrations used in these experiments, and the variation in intensity upstream and downstream of a stuck particle was not found to be a significant source of error.

ACKNOWLEDGMENTS

This work was supported by the US National Institutes of Health under Grant No. 1R01GM106420-01. Experiments were performed in the Nanobiotechnology Center Shared Research Facilities at Cornell.

APPENDIX: NOTES ON THE SUPPLEMENTAL MOVIE

The movie (see the Supplemental Material [35]) illustrates a raw experimental data set played back in real time. All light observed is scattered light collected through a microscope objective and imaged on a CMOS camera, as explained above. The images are acquired at 3000 frames per second. The video is played back in real time; the actual speed of the experiment is shown. The particles are 799-nm-diam polystyrene NIST traceable beads as described above. The experiment was performed in a dilute solution of KCl with $\lambda_D = 50$ nm. An exposure time of 24 μs was used for the camera.

[1] E. C. Dreaden, A. M. Alkilany, X. Huang, C. J. Murphy, and M. A. El-Sayed, Chem. Soc. Rev. **41**, 2740 (2012).
[2] H. Zhang, A. Nikolov, and D. Wasan, Energy & Fuels **28**, 3002 (2014).
[3] Y. Deng, A. Ediriwickrema, F. Yang, J. Lewis, M. Girardi, and W. M. Saltzman, Nat. Mater. **14**, 1278 (2015).
[4] H. Brenner, Chem. Eng. Sci. **16**, 242 (1961).
[5] A. J. Goldman, R. G. Cox, and H. Brenner, Chem. Eng. Sci. **22**, 637 (1967).
[6] A. J. Goldman, R. G. Cox, and H. Brenner, Chem. Eng. Sci. **22**, 653 (1967).
[7] R. G. Cox and H. Brenner, Chem. Eng. Sci. **22**, 1753 (1967).
[8] A. T. Clark, M. Lal, and G. M. Watson, Faraday Discuss. Chem. Soc. **83**, 179 (1987).
[9] G. D. M. MacKay, M. Suzuki, and S. G. Mason, J. Coll. Sci. **18**, 103 (1963).
[10] E. Schffer, S. F. Nrrelykke, and J. Howard, Langmuir **23**, 3654 (2007).
[11] M. D. Carbajal-Tinoco, R. Lopez-Fernandez, and J. L. Arauz-Lara, Phys. Rev. Lett. **99**, 138303 (2007).
[12] P. Huang and K. S. Breuer, Phys. Rev. E **76**, 046307 (2007).
[13] M. A. Brown and E. J. Staples, Langmuir **6**, 1260 (1990).
[14] M. A. Bevan and D. C. Prieve, J. Chem. Phys. **113**, 1228 (2000).
[15] N. A. Frej and D. C. Prieve, J. Chem. Phys. **98**, 7552 (1993).
[16] D. W. Pilat, B. Pouligny, A. Best, T. A. Nick, R. Berger, and H. J. Butt, Phys. Rev. E **93**, 022608 (2016).
[17] R. J. Oetama and J. Y. Walz, J. Colloid Interface Sci. **284**, 323 (2005).
[18] L. Liu, A. Woolf, A. W. Rodriguez, and F. Capasso, Proc. Natl. Acad. Sci. USA **111**, E5609 (2014).
[19] P. Schein, P. Kang, D. O'Dell, and D. Erickson, Nano Lett. **15**, 1414 (2015).
[20] S. Kawata and T. Sugiura, Opt. Lett. **17**, 772 (1992).
[21] D. Erickson, X. Serey, Y.-F. Chen, and S. Mandal, Lab Chip **11**, 995 (2011).
[22] H.-J. Wu, S. Shah, R. Beckham, K. E. Meissner, and M. A. Bevan, Langmuir **24**, 13790 (2008).
[23] P. Schein, C. K. Ashcroft, D. O'Dell, I. S. Adam, B. DiPaolo, M. Sabharwal, C. Shi, R. Hart, C. Earhart, and D. Erickson, J. Lightwave Technol. **33**, 3494 (2015).
[24] T. Brettschneider, G. Volpe, L. Helden, J. Wehr, and C. Bechinger, Phys. Rev. E **83**, 041113 (2011).
[25] Y. Kazoe, K. Mawatari, and T. Kitamori, Anal. Chem. **87**, 4087 (2015).
[26] K. D. Kihm, A. Banerjee, C. K. Choi, and T. Takagi, Exp. Fluids **37**, 811 (2004).
[27] A. Banerjee and K. D. Kihm, Phys. Rev. E **72**, 042101 (2005).
[28] P. Kang, P. Schein, X. Serey, D. O'Dell, and D. Erickson, Sci. Rep. **5**, 12087 (2015).
[29] J. Axelson, *USB Complete: The Developer's Guide* (Lakeview Research, Madison Wisconsin, 2015).
[30] M. Lindner, G. Nir, A. Vivante, I. T. Young, and Y. Garini, Phys. Rev. E **87**, 022716 (2013).
[31] D. C. Prieve, Adv. Colloid Interface Sci. **82**, 93 (1999).
[32] I. F. Sbalzarini and P. Koumoutsakos, J. Struct. Biol. **151**, 182 (2005).
[33] N. Chenouard, I. Smal, F. de Chaumont, M. Maska, I. F. Sbalzarini, Y. Gong, J. Cardinale, C. Carthel, S. Coraluppi, M. Winter, A. R. Cohen, W. J. Godinez, K. Rohr, Y. Kalaidzidis, L. Liang, J. Duncan, H. Shen, Y. Xu, K. E. G. Magnusson, J. Jalden, H. M. Blau, P. Paul-Gilloteaux, P. Roudot, C. Kervrann, F. Waharte, J.-Y. Tinevez, S. L. Shorte, J. Willemse, K. Celler, G. P. van Wezel, H.-W. Dan, Y.-S. Tsai, C. O. de Solorzano, J.-C. Olivo-Marin, and E. Meijering, Nat. Meth. **11**, 281 (2014).
[34] A. Gondarenko, J. S. Levy, and M. Lipson, Opt. Express **17**, 11366 (2009).
[35] See Supplemental Material at http://link.aps.org/supplemental/10.1103/PhysRevE.93.062139 for a video of an experimental data acquisition.